Measurement of $K^-p \to \eta\Lambda$ near threshold

A. Starostin,* B. M. K. Nefkens, E. Berger,† M. Clajus, A. Marušić,‡ S. McDonald, N. Phaisangittisakul, S. Prakhov, J. W. Price, M. Pulver, W. B. Tippens, and C. W. Wong
University of California, Los Angeles, California 90095-1547

D. Isenhower and M. Sadler
Abilene Christian University, Abilene, Texas 79699

C. E. Allgower§ and H. Spinka
Argonne National Laboratory, Argonne, Illinois 60439

J. R. Comfort, K. Craig, and A. F. Ramirez
Arizona State University, Tempe, Arizona 85287-1504

W. J. Briscoe and A. Shafi
The George Washington University, Washington D.C. 20052

D. M. Manley and J. Olmsted
Kent State University, Kent, Ohio 44242-0001

H. M. Staudenmaier
Universität Karlsruhe, Karlsruhe D-76128, Germany

D. Peaslee
University of Maryland, College Park, Maryland 20742-3255

V. Bekrenev, A. Koulbardis, N. Kozlenko, S. Kruglov, and I. Lopatin
Petersburg Nuclear Physics Institute, Gatchina RU-188350, Russia

N. Knecht, G. Lolos, and Z. Papandreou
University of Regina, Saskatchewan, Canada S4S OA2

I. Supek
Rudjer Boskovic Institute, Zagreb 10000, Croatia

D. Grosnick, D. Koetke, R. Manweiler, and S. Stanislaus
Valparaiso University, Valparaiso, Indiana 46383

(The Crystal Ball Collaboration)
(Received 31 May 2001; published 18 October 2001)

We present measurements of the differential and total cross sections and the Λ polarization for the reaction $K^-p \to \eta\Lambda$ from threshold to $p_{K^-} = 770$ MeV/c, with much better precision than previous measurements. Our cross-section data show a remarkable similarity to the SU(3) flavor-related $\pi^-p \to \eta n$ cross-section results. The reaction $K^-p \to \eta\Lambda$ at threshold is dominated by formation of the intermediate $\Lambda(1670)\frac{1}{2}^-$ state.

DOI: 10.1103/PhysRevC.64.055205 PACS number(s): 14.20.Jn, 13.75.Jz, 13.30.Eg, 24.85.+p

*On leave from Petersburg Nuclear Physics Institute, Gatchina, Russia.
†Present address: Division of Physics, Mathematics, and Astronomy, California Institute of Technology, MS105-24, 1200 E. California Blvd., Pasadena, CA 91125.
‡Present address: Collider-Accelerator Department, Brookhaven National Laboratory, Upton, NY 11973.
§Present address: Indiana University Cyclotron Facility, 2401 Milo B. Sampson Ln., Bloomington, IN 47405.

I. INTRODUCTION

New measurements of hyperon properties are much needed for investigating the consequences of the broken flavor symmetry of QCD. Flavor symmetry holds in the limit where the quarks have zero or the same mass. In that (unphysical) case, all quarks have identical strong interactions, which gives rise to novel relations between different reactions that have the same SU(3) flavor makeup. In reality the u quark mass is approximately 4 MeV, the d quark about 8 MeV and the s quark nearly 150 MeV. The characteristic hadronic scale is 1 GeV. It means that flavor symmetry can be expected to be applicable to systems of three light quarks, and the correction for the flavor-symmetry-breaking quark mass difference is tolerably small. Good examples of the use of broken flavor symmetry are the Gell-Mann decuplet and the Gell-Mann-Okubo octet mass relations.

In this paper we investigate whether the features of η threshold production in $\pi^- p$ interactions are also seen in $K^- p$ interactions, as expected from flavor symmetry. η is a special particle from an experimentalist's perspective because η can be detected cleanly over the full angular range by its characteristic decay into $\gamma\gamma$ and $3\pi^0$. η has the added advantage of isospin selectivity: $\pi^- p \to \eta n$ is pure $I=1/2$, while $\pi^- p$ elastic scattering requires both $I=1/2$ and 3/2 amplitudes. Similarly $K^- p \to \eta\Lambda$ is pure $I=0$, but $K^- p$ elastic scattering concerns $I=0$ and 1 amplitudes.

We have used the Crystal Ball high acceptance multiphoton spectrometer for an experiment at the Alternating Gradient Synchrotron at Brookhaven National Laboratory (BNL-AGS) in the low-energy separated K^- beam to measure $K^- p \to neutrals$. All neutral final states, such as $\pi^0\Lambda$, $\pi^0\pi^0\Lambda$, and $\pi^0\Sigma^0$, were measured simultaneously. We present here the first set of results, namely, η production by K^- on a proton target. We have obtained extensive data on σ_{total}, $d\sigma/d\Omega$, and Λ polarization for $K^- p \to \eta\Lambda$ from threshold to $p_{K^-}=770$ MeV/c. We compare our results with existing data on $\pi^- p \to \eta n$ to probe the role of flavor symmetry.

II. THEORY

The Lagrangian of QCD may be written as the sum of two components that have very different properties

$$\mathcal{L}_{QCD} = \mathcal{L}_0 + \mathcal{L}_m . \tag{1}$$

$\mathcal{L}_0$ depends on the quark and gluon fields, Ψ_q and A_μ, on their derivatives, and on one universal coupling constant g_s. $\mathcal{L}_0$ obeys flavor symmetry, which means that the strength of the strong interaction between the six different quark flavors is the same in the limit of massless quarks. The flavor symmetry is broken by the mass term

$$\mathcal{L}_m = -\overline{\Psi}_u m_u \Psi_u - \overline{\Psi}_d m_d \Psi_d - \cdots . \tag{2}$$

The significance of this mass term in comparison to $\mathcal{L}_0$ depends on the magnitude of the quark masses in the reaction being studied. For systems containing one or more u or d quarks, flavor symmetry is known as isospin symmetry, and its validity is well established [1]. When an s quark is involved, flavor symmetry is known as $SU(3)_f$ and it has not been investigated extensively.

Our new Crystal Ball data on η production by K^- provide a good opportunity for testing the usefulness of broken $SU(3)_f$ symmetry. To do so, we compare η production by K^- and π^-. The reaction

$$\pi^- p \to \eta n, \tag{3}$$

just above threshold is characterized by several special features:

(1) The total cross section for $\pi^- p \to \eta n$ increases as rapidly as allowed for s-wave production over the π^- beam momentum range from threshold to 50 MeV/c above [2]. In this region the total cross section rises linearly

$$\sigma_{total}(\pi^- p \to \eta n) = (21.2 \pm 1.8)\ \ \mu\text{b}/(\text{MeV}/c)\, p_\eta^* , \tag{4}$$

where p_η^* is the η momentum in the center of mass (c.m.) in MeV/c.

(2) The total cross section for η production has a maximum of 2.6 ± 0.3 mb, which is 7% of the total $\pi^- p$ cross section [3].

(3) The reaction $\pi^- p \to \eta n$ mainly proceeds via the intermediate production of the $N(1535)\frac{1}{2}^-$. The branching ratio for $N(1535)\frac{1}{2}^- \to \eta N$ is 35–55 %, which is comparable to the $N(1535)\frac{1}{2}^-$ decay into πN. Phase-space considerations imply that the ηN branch should be smaller than the πN branch.

(4) The angular distribution for $\pi^- p \to \eta n$ has a shallow minimum near 90° in the c.m. frame [4]. This feature is indicative of a small d-wave contribution, presumably due to the excitation of the $N(1520)\frac{3}{2}^-$.

(5) The ηN scattering length is large and attractive [5];

$$a_{\eta N} = [0.621 \pm 0.040 + i(0.306 \pm 0.034)]\ \text{fm}. \tag{5}$$

The above-mentioned features are consistent with η production near threshold occurring predominantly via the $N(1535)\frac{1}{2}^-$ intermediate state:

$$\pi^- p \to N(1535)1/2^- \to \eta n. \tag{6}$$

An $SU(3)_f$ analog of this reaction is

$$K^- p \to \Lambda(1670)1/2^- \to \eta\Lambda. \tag{7}$$

Assuming that the $N(1535)\frac{1}{2}^-$ and $\Lambda(1670)\frac{1}{2}^-$ are traditional three-quark states, flavor symmetry implies that threshold η production by π^- and K^- should have qualitatively similar features. The threshold for η production calculated using the η mass of 547.30 MeV [6] is at 684.5 MeV/c lab momentum for π^- and 722.1 MeV/c for K^-.

An alternative description of the $N(1535)\frac{1}{2}^-$ has been put forward by Kaiser *et al.* [7], in which the $N(1535)\frac{1}{2}^-$ is mainly a quasibound $K\Sigma$-$K\Lambda$ state. If this is the case, the

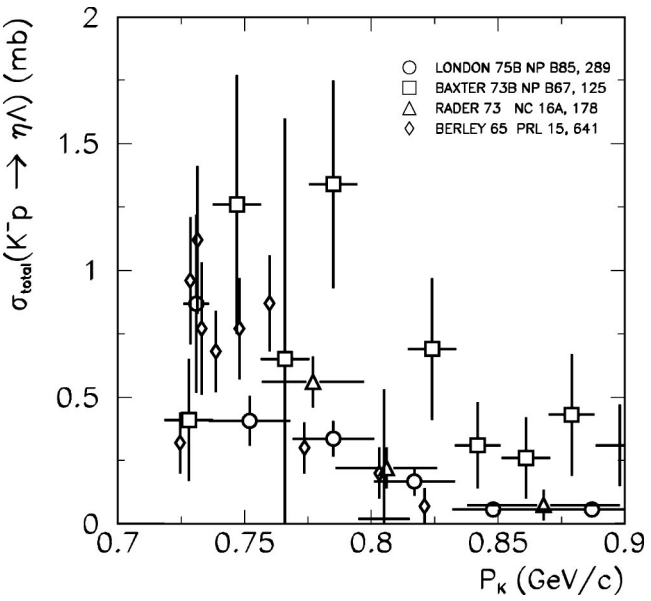

FIG. 1. The experimental data for the $K^-p\to\eta\Lambda$ total cross section [8–11] before this experiment.

$\Lambda(1670)\frac{1}{2}^-$ is not simply related to the $N(1535)\frac{1}{2}^-$, and there is no prediction regarding the relations for the threshold productions. This case is an illustration of the use of $SU(3)_f$ to distinguish between different models for baryons. This ability is of importance when searching for the elusive hybrid baryons.

The existing data on η production by K^- are meager [8–11]. They come from old bubble-chamber and spark-chamber experiments with very limited statistics. Figure 1 shows the experimental data for $\sigma_{total}(K^-p\to\eta\Lambda)$ before the present work.

III. EXPERIMENTAL EQUIPMENT

A. Outline

Approximately 2/3 of all η decays result in multiple photon final states and 1/3 of the Λ decays yield $\pi^0 n$. The detector of choice for $K^-p\to\eta\Lambda$ is a 4π-acceptance multiphoton spectrometer with good energy and angular resolutions, which permits an overconstrained determination of the reaction. The incident K^- beam should preferably be a particle separated beam with individually tagged kaons. Such is available at the BNL-AGS in the $C6$ line.

Our experimental setup is illustrated in Fig. 2. The elements shown are the downstream part of the $C6$ beam line after the second separator, the beam collimators, the Crystal Ball multiphoton spectrometer in its stand, the beam counters, beam wire chambers operating in the drift mode, a Cerenkov counter, and the beam stop. The Crystal Ball is outfitted with a liquid-hydrogen target located in its center. The target is surrounded by a cylinder made of scintillation counters to veto charged particles.

B. The $C6$ beam line

The $C6$ beam line at the AGS provides a separated beam of pions, kaons, and antiprotons. The maximum useful momentum of the beam line is 770 MeV/c. The beam line has two dipoles $D1$ and $D2$, seven quadrupoles $Q1-Q7$, two $\vec{E}\times\vec{B}$ field separators, and a "mass slit." $D1$ selects the polarity and momentum of the channel. The mass slit consists of a pair of tungsten jaws that are vertically adjustable. They are located at the vertical focus of the beam in the aperture of $Q5$ downstream of the two $\vec{E}\times\vec{B}$ field separators. The last two quadrupoles, $Q6$ and $Q7$, and the wedge dipole magnet $D2$ provide the final control of the kaon beams on the target. They are also used as a momentum spectrometer to determine the momentum of the kaons individually. The incident kaons were tracked by using seven beam wire chambers, which provided the track information necessary to make the momentum determination. They also give the kaon's x and y coordinates, which were used to calculate the impact trajectory in the target for each kaon. An eight-element horizontal hodoscope $S1$ was mounted immediately upstream of the first wire chamber to resolve multiple hit ambiguities arising from the high instantaneous rate in this region. The signals from the hodoscope counters were combined in a logical sum allowing only one element of the hodoscope to fire within a 6-ns time window (XOR). The beam intensity was monitored using the hodoscope $S1$, counter $S2$ ($12.7\times7.6\times0.3$ cm^3) located 314 cm upstream of the target, and timing counter ST ($7.6\times5.2\times0.6$ cm^3) located 163 cm upstream of the target. A beam halo (BH) detector, consisting of four scintillation paddles BH1–BH4 covering the beam halo, was located 145 cm upstream of the target. It defined a 6.1×4.6 cm^2 rectangular aperture for the beam. The BH signal was formed as a logical sum (OR) of the four halo veto counters.

A 61-cm-thick steel wall, which had a cylindrical steel insert with a 10-cm-diameter aperture, was located immediately downstream of $Q7$ and provided the primary shielding from beam-related background. There was a second wall made of 61-cm-thick concrete; it contained a lead insert with a 20-cm-wide by 10-cm-high aperture, to shield the spectrometer against beam scattering in the steel collimator and against particles from kaon decay in the beam. This wall was located 93 cm downstream of the primary wall. Another concrete wall was located immediately upstream of the gas Cerenkov counter to shield the experiment from the backscattered particles emanating from the beam stop. The cylindrical gas Cerenkov counter was 25 cm in diameter and 128 cm long; it was used to measure the electron contamination of the beam. A $15.2\times15.2\times1.9$ cm^3 scintillator located behind the Cerenkov counter defined the beam for the monitoring of the electron contamination during our pion runs.

Our $K^-p\to\eta\Lambda$ data were taken at two different beam momenta. The low- and high-momentum beams had central momenta of 720 MeV/c and 750 MeV/c, respectively. We used the beam chambers to measure the momentum difference of every K^- with respect to the central value. The momentum distributions of both K^- beams are shown in Fig. 3. The precision of the relative K^- momentum determination is ±2 MeV/c, and limits the size of the bins into which we

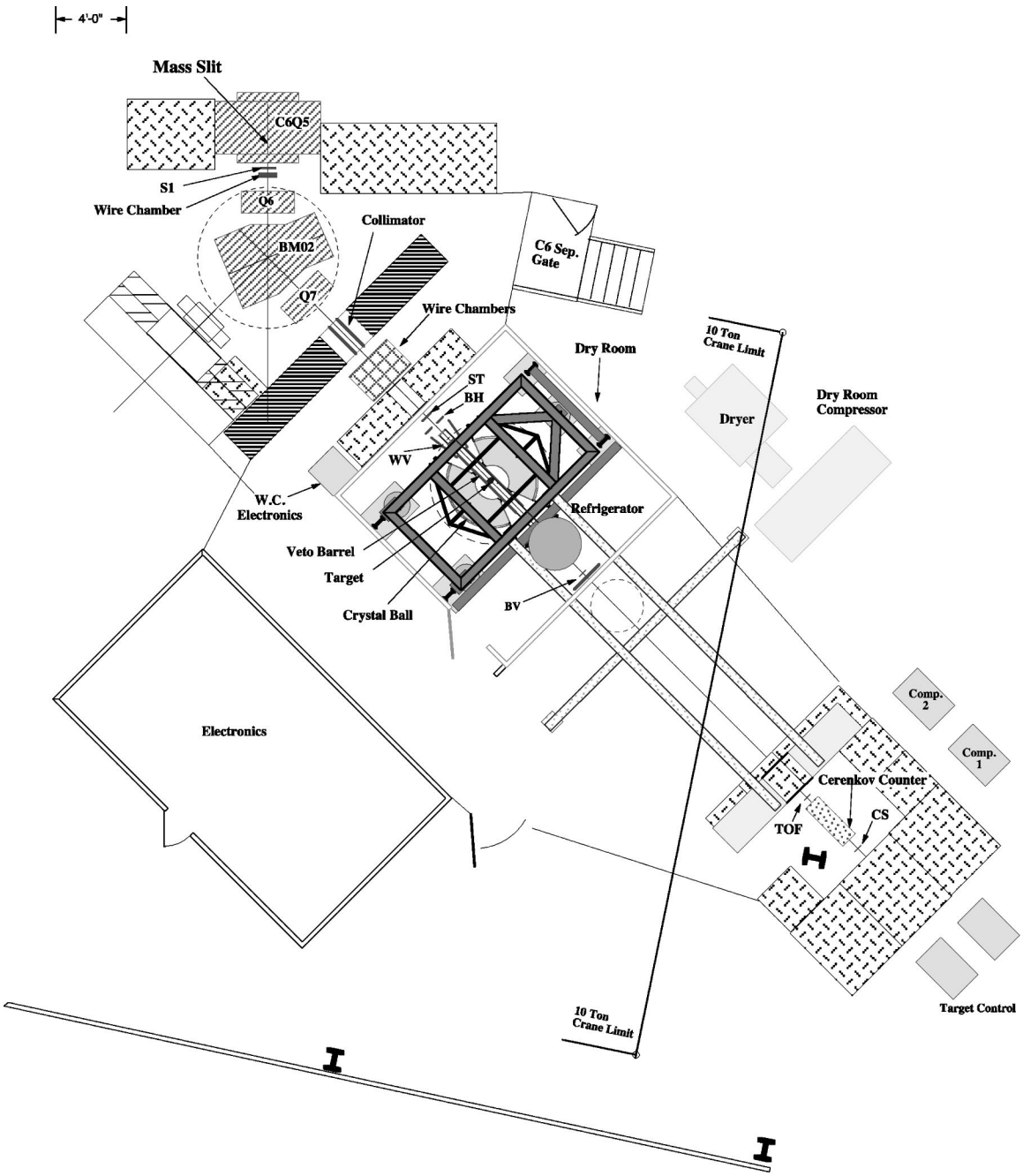

FIG. 2. Floor plan showing the *C*6 beam line downstream of the particle velocity separators and the experimental apparatus.

subdivided the entire beam to obtain the σ_{total} excitation function.

The absolute beam momentum was obtained from a detailed analysis of the η threshold production as discussed in Sec. VII. The accuracy of the absolute K^- momentum is ± 2.5 MeV/c. The beam momentum obtained by this method agrees by $\pm 0.5\%$ with the calibration of the $D2$ bending magnet from pions, as described in Ref. [12].

Both the low- and high-momentum beam were tuned to optimize the K-to-π ratio and the beam position on the target. We obtained about 8×10^4 kaons in an AGS beam spill of 2.8 s duration every 5 s with the K-to-π ratio about 1:10.

C. The Crystal Ball spectrometer

The Crystal Ball (CB) was built by Stanford Linear Accelerator Center (SLAC) [13]. The CB is made of 672 optically isolated NaI(Tl) crystals, 15.7 radiation lengths (r.l.) thick. The counters are arranged in a spherical shell with an inner radius of 25.3 cm and an outer radius of 66.0 cm. The hygroscopic NaI is housed in two hermetically sealed evacuated hemispheres. The CB geometry is based on that of an icosahedron. Each of the 20 triangular faces (''major triangles'') is divided into four ''minor triangles,'' each of which consists of nine crystals. This results in a total of 720 crystals, but 48 crystals were not installed to allow for en-

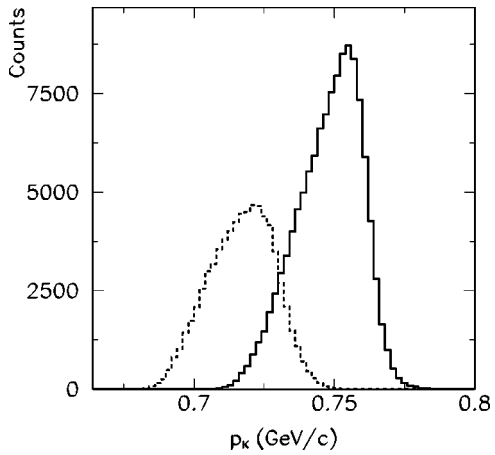

FIG. 3. The momentum distribution of the low-momentum beams (dashed line) and the high-momentum beams (solid line).

trance and exit tunnels. Each crystal is shaped like a truncated triangular pyramid, 40.6 cm high, pointing towards the center of the Crystal Ball. The base of each pyramid is an approximately equilateral triangle of about 12.7 cm and the apex is a 5.1 cm equilateral triangle (see Fig. 4). The geometrical considerations of constructing a solid spherical detector from such shapes requires the use of 11 slightly different pyramids, varying in size by a few percent. Each crystal is individually wrapped in reflective paper and aluminized mylar. It is viewed by its own SRC L50 B01 photomultiplier tube, which is a 5.1-cm-diameter, selected for linearity over a wide dynamic range. The phototube is connected to the crystal by a glass window and a 5 cm gap between the glass window and the crystal. The crystals are stacked so as to form top and bottom hemispheres, which are mechanically separated. The boundary between the two hemispheres is called the equator region and consists of two 0.76 mm stainless steel plates separated by 5 mm of air. This separation introduces an inactive space amounting to 1.6% of 4π. The inner wall of the hemisphere is 1.5 mm stainless steel or 0.09 r.l. The entrance and exit tunnels for the beam reduce the acceptance by 6.7%. The Crystal Ball resides in a dry room as a safeguard in case of a leak. The dry room is maintained at constant temperature, $(20\pm1)\,^{\circ}\mathrm{C}$, in a low humidity environment. The dry room was equipped with beam-entrance and beam-exit mylar windows.

A liquid-hydrogen target was installed at the center of the ball. The target flask is a horizontal cylinder 10.27 cm in diameter with spherical endcaps. The maximum length of the flask along the beam axis is 10.57 cm. The flask is surrounded by 40 layers of superinsulation on the sides and 15 layers over the endcaps. It is supplied by two thin feeding tubes from a hydrogen liquefier, which is located outside the dry room. The target is mounted inside a 7.4-cm-radius vacuum pipe that extends through the entrance and exit tunnels of the CB. The beam enters the vacuum pipe through a window in the upstream face made of 0.254-mm-thick mylar, and 0.305 mm Kevlar. The temperature and the pressure in the target are recorded approximately every 5 s during data acquisition.

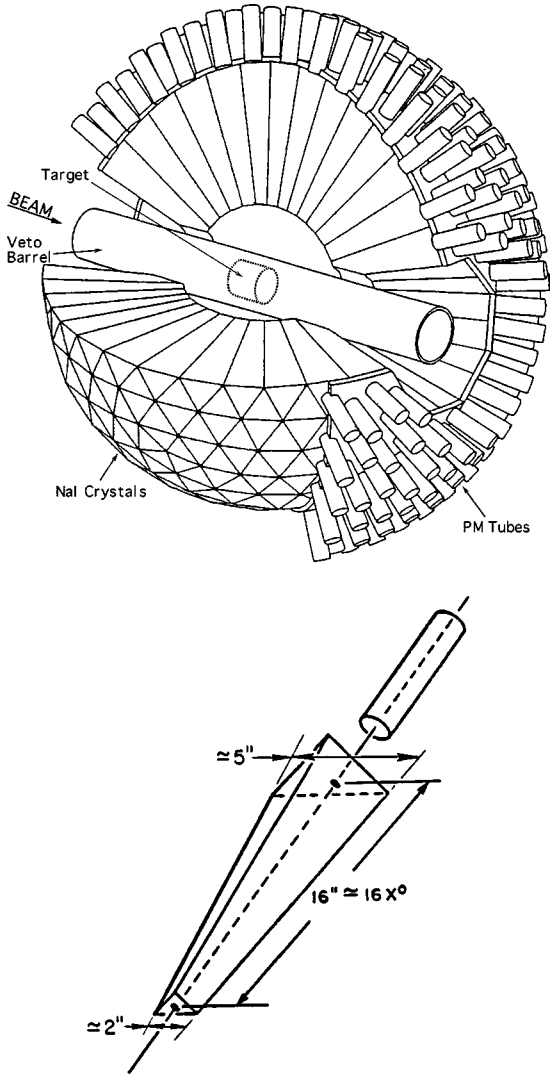

FIG. 4. In the upper figure is the layout of the Crystal Ball detector. In the lower figure are the dimensions of the Crystal Ball crystals [13].

The vacuum pipe is surrounded by a veto barrel (VB) made of four double-ended plastic scintillation counters, 120 cm long and 5 mm thick. These segments were made of BC412 bent cast sheets and are equipped with 35-cm-long plastic lightguides. Each scintillator and lightguide assembly is wrapped in sheets of mylar. The scintillators are coupled at each end to a Philips 2″ XP2230/H photomultiplier. A coincidence was formed between the signals from both ends of each counter. The VB signal was defined as the logical sum of the coincidences of all four counters. The entrance tunnel of the CB is covered by four trapezoidal veto counters WV; each counter is viewed by a single photomultiplier through a wavelength-shifting plastic lightguide. These counters were used primarily to veto muons from kaons decaying in flight. The WV signal was formed as a logical OR of the four WV counters. A beam veto counter BVS $(10.0\times10.0\times0.5\ \mathrm{cm}^3)$ located 211 cm downstream of the target was dedicated as a veto for beam particles that passed through the target without an interaction. A veto counter BV

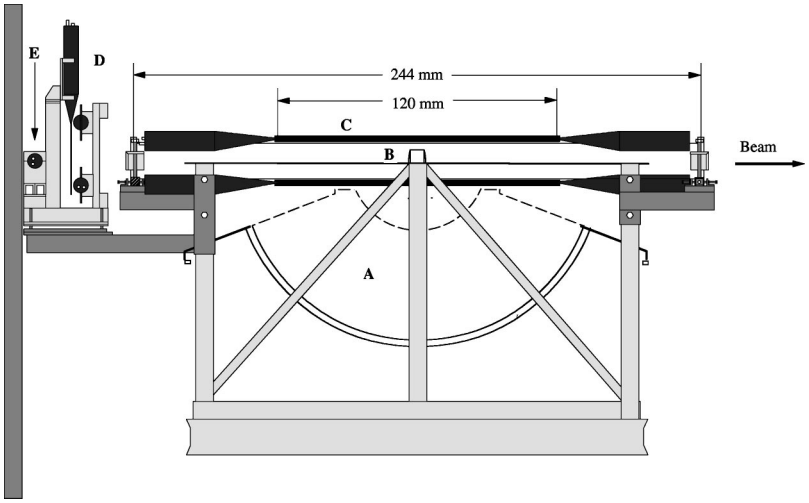

FIG. 5. Elevation view of the Crystal Ball detector showing the lower hemisphere NaI crystals (a), the LH_2 target (b), the veto barrel assembly (c), the beam halo veto detector (d), with the beam counter *ST* (e).

($55.0\times105.0\times0.5$ cm^3) used to veto the charged final states in the CB was located 221 cm downstream of the target. The BV and BVS counters were not in the trigger but their amplitudes and firing times were recorded.

Figure 5 shows the lower hemisphere of the CB together with the VB assembly, the BH detector, and the *ST* counter as they are arranged on the support stand in the CB dry room.

D. Trigger and read-out electronics

Several types of event triggers were recorded during data acquisition. A BEAM event trigger was formed by a coincidence of the XOR signal from the *S*1 hodoscope and the signals from the *S*2 and *ST* counters. The good time-of-flight (TOF) separation between pions and kaons in the beam allowed the electronic rejection of pions from the BEAM coincidence signal by choosing the proper relative delay between *S*1 and *ST*. The TOF spectrum of one of the *S*1 counters after the suppression of the pions is shown in Fig. 6. A CB event required the total energy deposited in the Crystal Ball to be greater than 350 MeV. This total energy excludes the energy deposited in the crystals around the tunnels. A CB_NEUTRAL event trigger was generated by a coincidence of a BEAM event, a CB event, and an anticoincidence of the BH, WV, and VB signals. A CB_CHARGED event trigger was defined as a coincidence of a BEAM event, a CB event, and a VB signal, in anticoincidence with BH and WV. All CB_NEUTRAL triggers, one out of 20 CB_CHARGED triggers, and one out of 2000 BEAM triggers were recorded during data taking.

The output of every crystal was sent to an Integrate-and-Hold (IH) module. These modules integrated the signals during a 350 ns gate and held them for digitization by the ADC if the trigger criteria were met. In each IH module, the signal was split to have two ranges: one for the high-range signal, which was attenuated by a factor of two, and one for the low range signal, which was amplified by a factor of ten. Both ranges were recorded as part of the data taking. The combination of the two ranges provided high resolution over a wide range of photon energies, from ~1 MeV to 1 GeV. Part of the signals from the crystals were used to generate the energy sum for every minor triangle and the total energy in the Ball. The total energy sum was used in the trigger. The energy sum signal of every minor triangle was used for timing. We recorded the timing information associated with each of the 80 CB minor triangles by using multihit TDC's. This information was used in the offline analysis to reject hits in the CB coming from out-of-time accidentals. A PULSER event initiated the readout of all ADC channels of the ADC pedestals. The PULSER event was generated approximately once per second during data taking. Additionally the energy background in the crystals during the beam spill was determined from a comparison of the PULSER data *in* and *out* of the beam spill. The information about the background energy was used in our Monte Carlo simulation of the experiment (see Sec. V C).

Our data acquisition system (DAQ) used the CODA package developed at JLab [14]. The practical data acquisition rate was about 300 events per second, which allowed us to

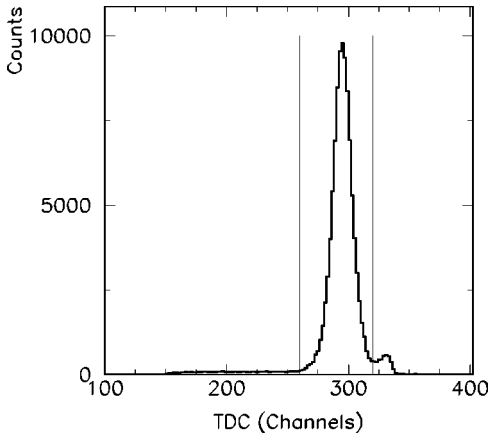

FIG. 6. TOF spectrum *ST*–*S*1 for one of the *S*1 hodoscope counters of the high-momentum beam after pion suppression. The abscissa shows the inverse time scale of 50 ps/channel. The peak is the kaon TOF. Without hardware suppression pions would have peaked around channel 350 in this plot. The two vertical lines show the TOF cut that was used to calculate the number of kaons in the beam.

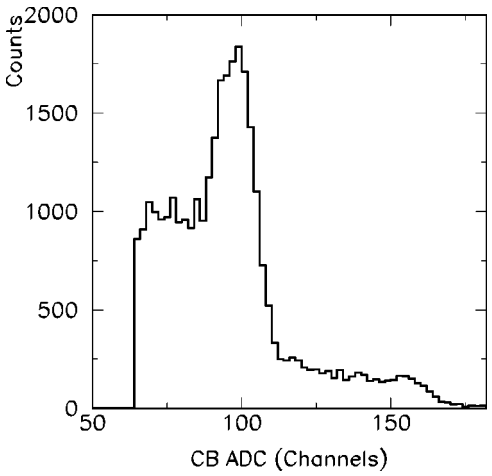

FIG. 7. Typical ^{60}Co spectrum of a CB crystal.

keep the live time of the DAQ system during data taking at about 70%.

IV. CALIBRATION OF THE CRYSTAL BALL

An initial relative hardware calibration of the crystals was made by using a radioactive source. A typical spectrum from a single NaI counter obtained with a ^{60}Co source is shown in Fig. 7. The absolute energy calibration uses the invariant masses of the $\pi^0 \to \gamma\gamma$, $\eta \to \gamma\gamma$, and $\eta \to 3\pi^0$ processes. An example of the experimental resolution obtained in a series of pion runs with a thin CH_2 target is shown in Fig. 8. The figure shows the distribution of the invariant mass for two photons obtained for the CH_2 target after subtraction of the normalized carbon and empty target data. The first peak in the spectrum has a centroid equal to the π^0 mass and a width with $\sigma = 11.5$ MeV. This peak arises from the $\pi^- p \to \pi^0 n$ reaction. The second peak has a centroid equal to the η mass and a width with $\sigma = 18.0$ MeV. It is due to $\pi^- p \to \eta n$ followed by the $\eta \to \gamma\gamma$ decay.

The relative resolution of each crystal was extracted from the data obtained during a special run with K^+ mesons that stopped in a plastic target located in the center of the Crystal Ball. The peak from the monoenergetic muons produced by $K^+ \to \mu^+ \nu_\mu$ at rest is shown in Fig. 9. We collected ~ 200 events per crystal with a muon depositing more than 90% of its energy in a single crystal. The relative width of the peak in percent for each individual crystal was obtained from such events. The measured width for all crystals is summarized in a frequency plot in Fig. 10.

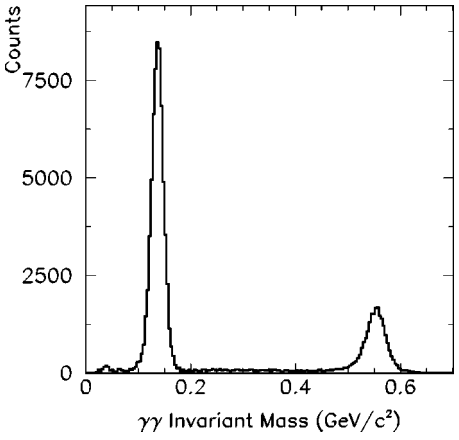

FIG. 8. Invariant mass of two photons obtained for a 1.8-cm-thick CH_2 target in a 750 MeV/c π^- beam. The normalized carbon and empty target spectra have been subtracted.

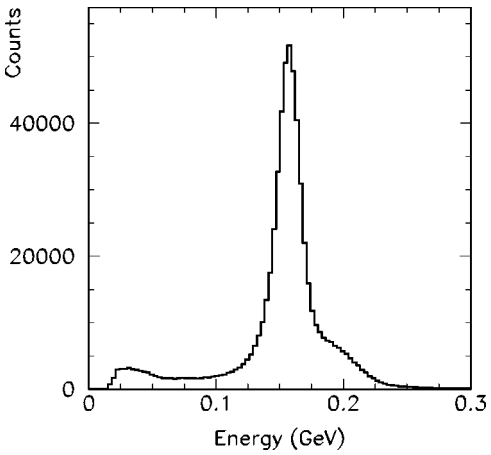

FIG. 9. The energy of single charged particles in the Crystal Ball obtained with stopped K^+ mesons. The peak is due to the monoenergetic muons from the $K^+ \to \mu^+ \nu_\mu$ decay at rest. The shoulder on the right side of the peak is due to the $\mu^+ \to e^+ \nu_e \bar{\nu}_\mu$ decay.

The energy resolution of the CB for electromagnetic showers depends on the remnant light in the NaI crystals from earlier particles. It is a function of the beam intensity and size. For a moderate intensity π^- beam the energy resolution is typically $\sigma_E/E \sim 2.0\%/[E\ \ (\mathrm{GeV})]^{0.36}$. The angular resolution for 50–500 MeV photon showers is $\sigma_\theta = 2° - 3°$ for the polar angle and $\sigma_\phi = 2°/\sin\theta$ for the azimuthal angle.

V. ANALYSIS

A. Event selection

The objective of this study is the $K^- p \to \eta\Lambda$ reaction. The final state was identified in two ways: (i) via the $\eta \to \gamma\gamma$ and

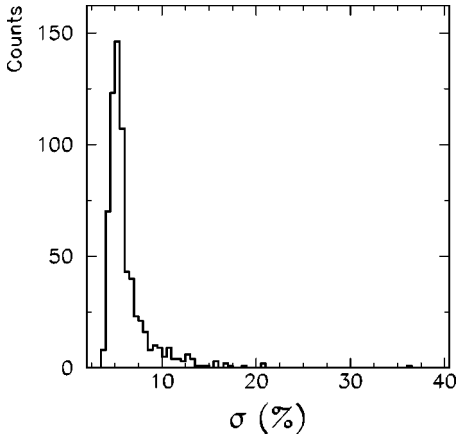

FIG. 10. Frequency distribution of the width of the energy spectra in the crystals produced by the monoenergetic muon, kinetic energy $E_\mu \approx 153$ MeV, from $K^+ \to \mu^+ \nu_\mu$ decay at rest.

$\Lambda \to \pi^0 n$ decays, labeled $K^- p \to \eta(2\gamma)\Lambda$; (ii) via $\eta \to 3\pi^0$ and $\Lambda \to \pi^0 n$, labeled $K^- p \to \eta(3\pi^0)\Lambda$. All crystals with an energy deposit in excess of 1 MeV were used in the analysis. We use the term ''cluster'' to refer to a group of 13 neighboring crystals in the CB with at least 15 MeV deposited in the central crystal. Each cluster is presumed initially to result from a single photon. Every crystal is assigned the TOF data associated with the minor triangle to which it belongs. If there is more than one TDC hit in a minor triangle, the latest TDC pulse was used. A crystal has good timing information if the TOF value is in a 20 ns time window generated by the incident K^-. We distinguish three types of events according to the timing properties: (i) All crystals in all clusters are in time. We have analyzed the four- and the eight-cluster events of this type; they are the basis for calculating the differential and the total cross sections and the Λ polarization. (ii) All central crystals of all clusters are in time, but one or more of the surrounding crystals of any of the clusters have a timing signal outside the 20 ns window. Such an event type is interpreted as a pileup of a $K^- p \to \eta\Lambda$ and a background event without producing an extra cluster in the CB (''energy pileup''). The four- and the eight-cluster events of this type were analyzed, and enabled us to calculate the correction for events lost due to the energy pileup. (iii) The third event type has one or more clusters whose timing signal of the central crystal is outside the 20 ns window. This indicates a pileup of a $K^- p \to \eta\Lambda$ and a background event with an extra cluster produced by the background event (''cluster pileup''). The total number of $K^- p \to \eta(2\gamma)\Lambda$ events was corrected for the cluster pileup based on the analysis of five-cluster events. All possible combinations of four clusters from the five-cluster events were analyzed as described below for the four-cluster neutral event type.

The neutrons from $\Lambda \to \pi^0 n$ usually escape through the exit tunnel of the CB. The number of the $K^- p \to \eta(2\gamma)\Lambda$ events with a neutron detected in the CB is estimated to be 7%. For the analysis we assumed that all clusters in the CB are due to photons. For the event selection we used a least squares fit with kinematical constraints. The fit included two free parameters: (i) the z coordinate of the primary interaction point along the trajectory of the beam particle in the target; (ii) the distance between the primary interaction point and the point of the Λ decay. For much of the analysis we used only four-cluster neutral events. In the first stage of the analysis, the two photons from the sequence $\Lambda \to \pi^0 n \to \gamma\gamma n$ were identified. We tested the six combinations of four clusters to the hypothesis $K^- p \to \gamma\gamma\Lambda$ followed by $\Lambda \to \pi^0 n \to \gamma\gamma n$. An event was accepted if exactly one of the combinations satisfied the $K^- p \to \gamma\gamma\Lambda$ hypothesis with a probability greater than 1%, i.e., with a 1% confidence level (CL). Figure 11 shows the invariant mass distribution of the two photons from $K^- p \to \gamma\gamma\Lambda$ events identified in the first stage. The spectrum shows two narrow peaks produced by $K^- p \to \pi^0\Lambda$ and $K^- p \to \eta(2\gamma)\Lambda$. The background under the η peak is estimated to be less than 5%. The main source of the background is $K^- p \to \pi^0\Sigma^0$ followed by $\Sigma^0 \to \gamma\Lambda$ decay. This background is suppressed in the second stage of the analysis, in which the events were fitted to the hypothesis $K^- p \to \eta\Lambda$ followed by $\Lambda \to \pi^0 n \to \gamma\gamma n$ and $\eta \to \gamma\gamma$. An event was accepted if the hypothesis was satisfied with a 5% CL. The total number of events selected for the high-momentum beam was about 2000; for the low-momentum beam the number was about 200. The empty target contribution to the $K^- p \to \eta(2\gamma)\Lambda$ sample was less than 2%.

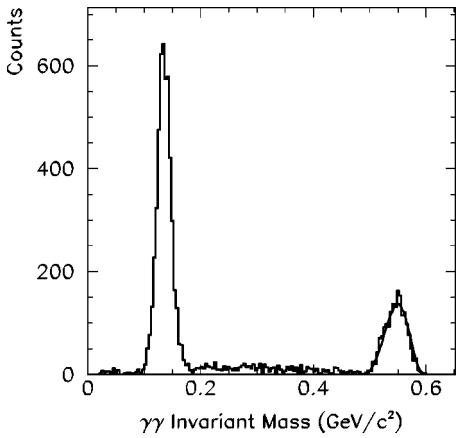

FIG. 11. The invariant mass of two photons in $K^- p \to \gamma\gamma\Lambda$ obtained with the high-momentum beam. The normalized empty target spectrum has been subtracted. The results of the Monte Carlo simulation are shown by the smooth solid line. The first peak is due to $K^- p \to \pi^0\Lambda$ and the second one to $K^- p \to \eta\Lambda$.

As an illustration of the quality of our data, the distribution of the distance between the primary interaction point in the target and the point of the Λ decay is shown in Fig. 12. This distribution was obtained for the high-momentum beam using the $K^- p \to \eta(2\gamma)\Lambda$ events. The distance was calculated as a free parameter of the kinematical fit procedure. The dashed line in Fig. 12 is the Monte Carlo result calculated for the decay $c\tau = 7.89$ cm.

We used the neutral eight-cluster events to identify the reaction $K^- p \to \eta\Lambda$ via the $\eta \to 3\pi^0$ decay. The analysis was performed in three steps. In the first step, the two photons from the Λ decay and the six photons from the η decay were identified. We analyzed all 28 possible combinations of eight

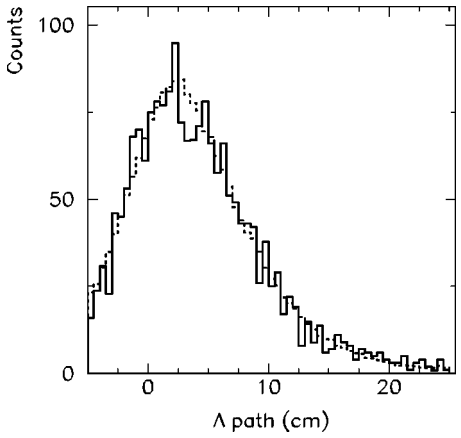

FIG. 12. The decay-distance distribution of the Λ in $K^- p \to \eta\Lambda$. The experimental result for the high-momentum beam is shown by the solid line. The Monte Carlo simulation is shown by the dashed line. The Λ decay distance used for the Monte Carlo is $c\tau = 7.89$ cm.

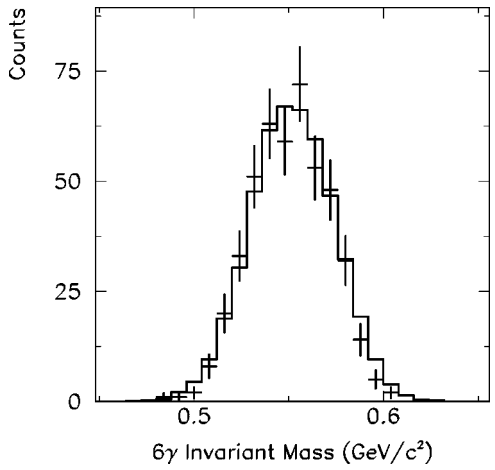

FIG. 13. The invariant mass of the six photons in $\eta \to 3\pi^0$ from $K^- p \to \eta\Lambda$ for the high-momentum beam. The experimentally measured distribution with its statistical uncertainty is shown by crosses, the result of the Monte Carlo simulation by the solid line.

clusters, testing the hypothesis $K^- p \to \eta\Lambda$ followed by the $\Lambda \to \pi^0 n \to \gamma\gamma n$ and $\eta \to 6\gamma$ decays. All combinations satisfying this hypothesis with a probability greater than 1% were used. In the second step, the Λ was reconstructed by using two photons identified in step one. For the remaining six photons we analyzed all 15 possible combinations in testing the $\eta \to 3\pi^0 \to 6\gamma$ hypothesis. All combinations satisfying the hypothesis $K^- p \to \eta\Lambda$ followed by $\Lambda \to \pi^0 n \to \gamma\gamma n$ and $\eta \to 3\pi^0 \to 6\gamma$ with a probability greater than 1% were selected. For further analysis we chose the combination with the highest probability. In the third step, the kinematical fit to the hypothesis $K^- p \to \eta\Lambda$ followed by $\Lambda \to \pi^0 n \to \gamma\gamma n$ and $\eta \to 3\pi^0 \to 6\gamma$ was made. The event was accepted if this combination satisfied the hypothesis with a 5% C.L. We have selected 450 such events for the high-momentum beam. Figure 13 shows the invariant mass distribution of the six photons from the $\eta \to 3\pi^0 \to 6\gamma$ decay of $K^- p \to \eta\Lambda$, compared to the results of a Monte Carlo simulation. The empty target contribution was less than 1%.

We have also reconstructed the events in which only one combination survived after the second step of the analysis. The invariant mass and the angular distributions of the η's from the unique combination are in agreement within the statistical accuracy with the results obtained from the best combination. We have used the results from the best combination because they have approximately three times higher statistics.

The event yield is subject to the following corrections:

(1) Dead time of the DAQ system ($\approx 33\%$).

(2) A correction due to the energy pileup in the CB. This correction was calculated by using the four-cluster and the eight-cluster events. The correction is 9.6% for the $K^- p \to \eta(2\gamma)\Lambda$ sample and 13.4% for $K^- p \to \eta(3\pi^0)\Lambda$.

(3) A correction for the cluster pileup in the CB. This correction was calculated for five-, six-, and seven-cluster events. The correction for the five-cluster events was obtained from all possible combinations of the five-clusters fitted to the $K^- p \to \eta(2\gamma)\Lambda X$ hypothesis for the cases where the central crystal of cluster X is out of time. The correction for the five-cluster events is $\approx 7\%$. The correction for the six- and seven-cluster events was estimated based on the correction factor obtained for the five-clusters and the total number of six- and seven-cluster events. The correction is 4% for six-cluster events, and 1% for the seven-cluster sample. The total correction to the number of good events due to the cluster pileup is calculated to be about 12%.

B. Number of kaons in the beam

The total number of kaons passing through the LH_2 target was calculated from the number of BEAM coincidences. This number was reduced for the following:

(1) The fraction of pions in the BEAM coincidence. The number of pions was determined from the BEAM events from the $S1$ TOF spectra. The cuts applied to one of the $S1$ TDC spectra are shown in Fig. 6. The events between the two solid lines are the kaons.

(2) Kaon decays between ST and the center of the LH_2 target ($\approx 21\%$). This number includes the kaons that decay before ST when a decay muon hits the ST counter. This correction was calculated by using a Monte Carlo simulation of the beam.

(3) The beam particles that missed the LH_2 target ($\approx 20\%$). This number was determined by using the x and y projections of the beam particle on the target from BEAM events.

(4) The number of kaons that scattered in the ST counter and material between the ST counter and the LH_2 ($\approx 3.5\%$). This number was calculated by using a Monte Carlo simulation of the beam.

(5) The number of pions under the kaon peak within the limits of the TOF cut ($\approx 5\%$). This number was obtained from an extrapolation of the pion background under the kaon peak (see Fig. 6).

(6) Inefficiency of the beam wire chambers ($\approx 49\%$).

The beam momentum distributions for both the low- and high-momentum beam were split into smaller momentum intervals. A beam momentum interval of 4 MeV/c was used for the $K^- p \to \eta\Lambda$ total cross and differential cross sections. For the Λ polarization data, larger momentum interval was used to reduce the statistical uncertainties. The number of kaons in each momentum interval is proportional to the number of the BEAM events in that interval.

C. The Monte Carlo simulation

We have used the GEANT 3.21 detector simulation package to make an extensive Monte Carlo simulation of our experiment. The simulated setup consists of the 672 crystals of the CB itself, grouped into minor and major triangles. Also included were the major parts of the CB enclosure such as the inner steel sphere and outer aluminum sphere, the cylindrical part of the beam entrance and exit tunnels, and the hexagonal ''skirts'' at the outer ends of the beam tunnels. The second part of the setup was the target assembly, consisting of the flask, the target material (e.g., LH_2), the beam pipe, the veto barrel counters, the halo veto counters and the wavelength-shift counters.

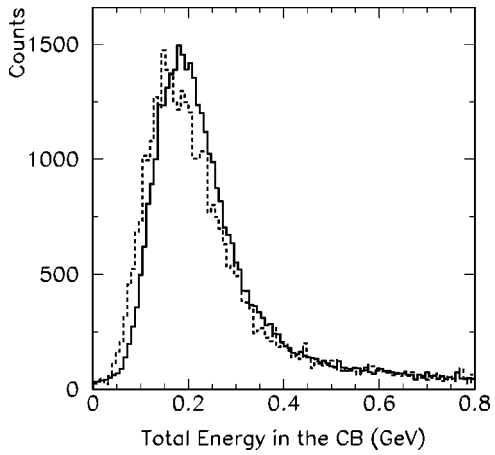

FIG. 14. The background energy in the CB measured for the kaon runs taken with the high-momentum beam. The energy is measured as the difference between the energy in all crystals *in* and *out* of the beam spill using the random PULSER event. The results obtained for the runs with full target are shown by the solid line; the empty target data by the dashed line. The empty target data have been multiplied by the ratio of the kaons fluxes of the full and empty target runs. The energy difference between the full and the empty target runs is due to the extra background energy coming from particle interactions in the LH_2.

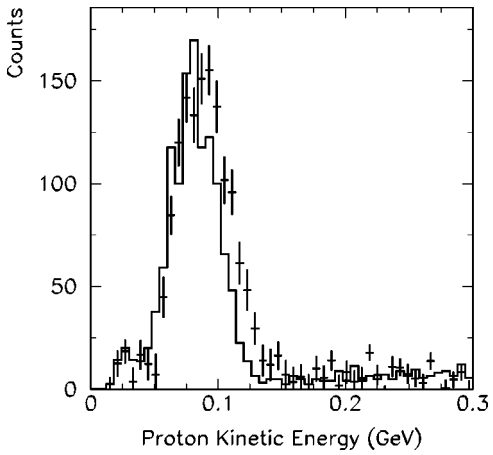

FIG. 15. The distribution of the proton kinetic energy in the c.m. frame for the $K^-p\rightarrow K^-p$ events for the high-momentum beam. The experimental data with their statistical uncertainties (crosses) are compared to the results of the $K^-p\rightarrow K^-p$ Monte Carlo simulation (solid line).

The details of the event simulation are as follows. We stored the trajectory of the incident K^- (its four momentum and the projected x and y coordinates in the LH_2 target) for each event in this experiment. These stored trajectories were used in our event simulation to generate the incident K^-. The kinematics of the reaction chain $[K^-p\rightarrow\eta(2\gamma)\Lambda$, or $K^-p\rightarrow\eta(3\pi^0)\Lambda]$ were generated based on the total and the differential cross-section distributions measured by us in this experiment. The simulation included the tracking of the neutron from the $\Lambda\rightarrow\pi^0 n$ decay by using the standard GEANT hadronic package. The random-energy background in the crystals was simulated by using the experimental data. Figure 14 shows the background energy in the CB, as determined from random PULSER events. It represents the difference in the sum of the energies over all crystals between an in-beam and the preceding out-of-beam PULSER events. The comparison of the spectra for the runs with the full and the empty target indicates that most of the background comes from the beam, i.e., it was produced by muons from the $K^-\rightarrow\mu^-\overline{\nu}_\mu$ decay of beam kaons. The average total background energy in the Ball was approximately 200 MeV, or $\approx$300 keV per crystal. The background energy in every crystal was stored event by event for each PULSER event. The energy was mixed with the Monte Carlo data when the data were analyzed.

The proper simulation of the veto barrel response is important for the interpretation of the results of this experiment. The simulation requires the energy calibration of the counters including the determination of the light attenuation function in the plastic material of the veto barrel. The exponential light attenuation function was determined in a separate measurement of $\pi^+p\rightarrow\pi^+p$ elastic scattering [15]. The veto barrel counters were calibrated by using $K^-p\rightarrow K^-p$ elastic scattering. The reaction was identified from two-cluster CB_CHARGED events that were consistent with two–body reaction kinematics. A signal from two veto barrel counters on opposite sides was required. The distribution of the c.m. kinetic energy of the proton produced in the $K^-p\rightarrow K^-p$ reaction for the high-momentum beam is shown in Fig. 15 and compared to the results of the $K^-p\rightarrow K^-p$ Monte Carlo simulation. The comparison shows that the $K^-p\rightarrow K^-p$ reaction is clearly identified and has less than 10% background. The slight difference in the peak positions in Fig. 15 could be explained by improper energy calibration of the CB for protons. Figure 16 shows the amplitude distribution for one of the veto barrel photomultipliers in units of ADC channels, obtained from the selected $K^-p\rightarrow K^-p$ events. The proton and kaon peaks are clearly visible in the spectrum. The positions of the peaks were used for the calibration of the veto barrel. In Fig. 16 the measured distribu-

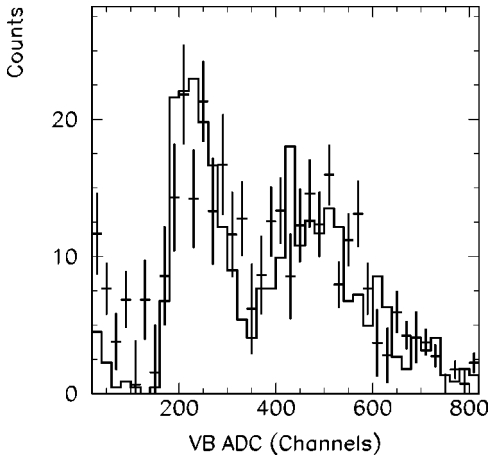

FIG. 16. Spectrum of the veto barrel ADC from one of the photomultipliers for $K^-p\rightarrow K^-p$ events. The data with the statistical uncertainties are shown by crosses. They are compared to the results of the Monte Carlo simulation shown by the solid line.

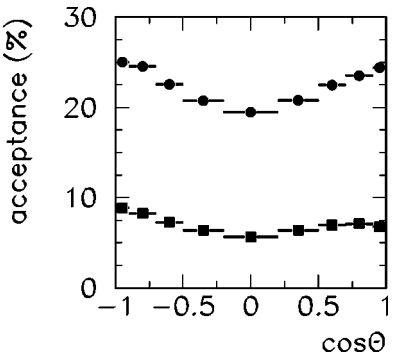

FIG. 17. CB acceptance for $K^- p \to \eta\Lambda$ calculated for the two major neutral η decay modes using the high-momentum beam. Circles represent $\eta \to \gamma\gamma$ and squares $\eta \to 3\pi^0$ decays.

tion is shown and compared to the Monte Carlo spectrum calibrated in ADC channels.

The results of the Monte Carlo simulation are shown in Figs. 11, 12, and 13, and compared to the experimental results. They agree within the experimental uncertainties. The Crystal Ball acceptance for the $K^- p \to \eta\Lambda$ reaction was calculated for both η decay modes (see Fig. 17). For both decay modes, the acceptance is a smooth function of $\cos\Theta$, where the angle Θ refers to the direction of the η with respect to the incident K^- in the the c.m. system. These functions were calculated separately for all our momentum intervals. We used nine bins for the $\cos\Theta$ axis. The number of bins reflects our angular resolution and limited statistics.

A separate beam simulation was performed to calculate the probability of the kaons rescattering in the ST counters and the probability of K^-/μ^- misidentification in the ST counter. The Monte Carlo simulation included all elements of the beam line after the last quadrupole $Q7$. The simulation was made from the parameters of the incident K^- beam recorded during the experiment.

VI. RESULTS

A. The total and differential cross sections

The number of protons in the LH_2 target was obtained from the known density of liquid hydrogen in the target and the average K^- path length through the hydrogen. The average K^- path length in the target was calculated from the measured trajectories of the beam particles and the geometry of the target. In this experiment the path length in the target was about 9.6 cm, or 91% of the maximum length of the target.

The total number of $\eta\Lambda$ events was calculated by taking into account the branching ratio of 35.8% for $\Lambda \to \pi^0 n$, and 98.8% for $\pi^0 \to \gamma\gamma$ [6]. We used BR($\eta \to \gamma\gamma$) = 39.33% and BR($\eta \to 3\pi^0$) = 32.24% [6].

The total cross section for the $K^- p \to \eta\Lambda$ reaction is shown in Fig. 18 and listed in Table I. The cross section was extracted using the $\eta \to \gamma\gamma$ decay mode for the two average beam momenta divided into 4 MeV/c wide momentum bins. The solid squares are the data obtained for the high-momentum beam, and the open squares show the data for the low-momentum beam. The data obtained with the low- and high-momentum beam show good agreement. The total cross sections for $K^- p \to \eta\Lambda$ obtained for the high-momentum beam for $\eta \to 3\pi^0$ are shown in Fig. 19. They are compared with the same distribution for the $\eta \to \gamma\gamma$ decay mode. The data obtained for the two η decay modes agree within their experimental uncertainties.

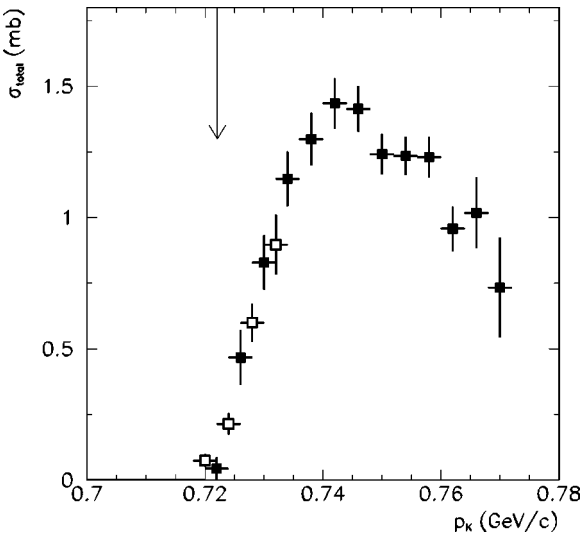

FIG. 18. The $K^- p \to \eta\Lambda$ total cross section measured as a function of the K^- momentum for the $\eta \to \gamma\gamma$ decay mode. The open squares (□) are for the low-momentum beam and the the solid squares (■) the high-momentum beam. The arrow indicates the threshold for $K^- p \to \eta\Lambda$ at 722 MeV/c.

The differential cross section $d\sigma/d\Omega$ was calculated for 4 MeV/c wide incident K^- momentum bins. The differential cross sections obtained for both low- and high-momentum beam for the $\eta \to \gamma\gamma$ decay mode are shown in Fig. 20 and listed in Table II. The differential cross sections extracted

TABLE I. $K^- p \to \eta\Lambda$ total cross section. The momentum intervals are 4 MeV/c wide. Uncertainties are statistical only.

p_{K^-} (MeV/c)	σ_{total} (mb)
720	0.07 ± 0.02
722	0.04 ± 0.04
724	0.21 ± 0.04
726	0.47 ± 0.10
728	0.60 ± 0.07
730	0.83 ± 0.10
732	0.90 ± 0.11
734	1.15 ± 0.10
738	1.30 ± 0.10
742	1.44 ± 0.10
746	1.41 ± 0.09
750	1.24 ± 0.08
754	1.23 ± 0.07
758	1.23 ± 0.08
762	0.96 ± 0.08
766	1.02 ± 0.13
770	0.73 ± 0.19

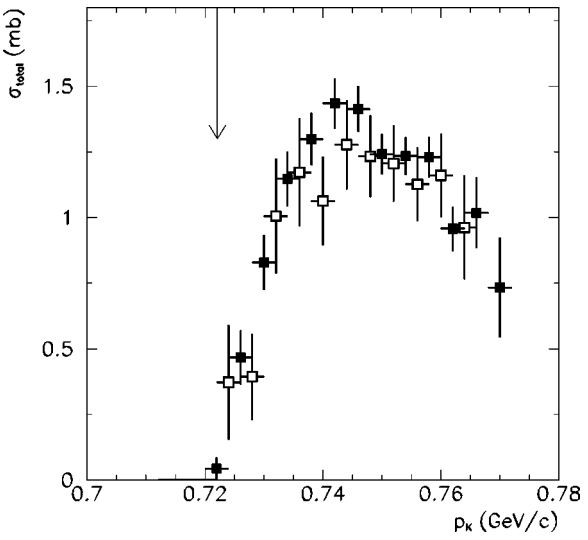

FIG. 19. The $K^- p \to \eta\Lambda$ total cross section measured as a function of the K^- momentum. The data are for the $\eta \to \gamma\gamma$ and $\eta \to 3\pi^0$ decay modes using the high-momentum beam. Cross sections obtained using $\eta \to 3\pi^0$ are shown by the open squares (□), and the results using $\eta \to \gamma\gamma$ are given by the solid squares (■). The arrow indicates the threshold for $K^- p \to \eta\Lambda$.

using the $\eta \to 3\pi^0$ decay mode for the high-momentum beam are also shown in Fig. 20 for comparison.

B. Calculation of the Λ polarization

The polarization of the Λ was determined from the asymmetry of the $\Lambda \to \pi^0 n$ decay

$$P_\Lambda(\cos\Theta) = 3\left(\sum_i \cos\xi_i\right) \Big/ \left[\alpha_\Lambda N(\Theta)\right], \tag{8}$$

where the angle ξ is defined as

$$\cos\xi = (\hat{K}\times\hat{\eta})\cdot\hat{\pi}/|\hat{K}\times\hat{\eta}| \equiv \hat{n}\cdot\hat{\pi}, \tag{9}$$

where $\hat{K}$, $\hat{\eta}$, and $\hat{\pi}$ are unit vectors in the direction of the incident K^-, the outgoing meson and the decay pion, respectively (in the Λ rest frame); $\hat{n}$ is the normal to the production plane. $N(\Theta)$ is the total number of Λ's produced at the angle Θ, and $\alpha_\Lambda = +0.65$ is the Λ asymmetry parameter [16].

The Λ polarization in $K^- p \to \eta\Lambda$ obtained from the $\eta \to \gamma\gamma$ decay mode for the high-momentum beam is shown in Fig. 21 and listed in Table III. The polarization is calculated in two momentum bins of 722–750 MeV/c and 750–770 MeV/c.

VII. EXPERIMENTAL UNCERTAINTIES

The uncertainty in the number of incident kaons is estimated to be 3%. The largest contributions to this uncertainty come from the uncertainty in the number of kaons rescattered between *ST* and the LH_2, and the uncertainty associated with extrapolation of the π^- background under the kaon peak in the *S*1–*ST* TOF spectra (see Fig. 6).

The uncertainty in the experimental acceptance mainly originates in the imperfect simulation of the veto barrel response function (see Sec. V C). The effect of this uncertainty on the differential and total cross sections was estimated by using the Monte Carlo simulation to study of the sensitivity of the cross sections to changes in the VB parameters. The VB thresholds are known to an accuracy of about ±10 ADC channels. That uncertainty leads to about a 4% variation in the differential and total cross sections. A 15% change in the light attenuation function results in about a 4% change in the values of the total and differential cross sections. The changes in the parameters of the VB do not affect the angular distributions within the statistical uncertainties.

The contribution of all possible sources of background to our event sample was estimated by using the data sample below the eta threshold for both η decay modes. The contribution of background events to the total cross section for $K^- p \to \eta(2\gamma)\Lambda$ is less than 25 μb. This corresponds to a relative uncertainty in the total cross section for $K^- p \to \eta(2\gamma)\Lambda$ from 5% at 726 MeV/c to about 1% at 742 MeV/c (see Table I). Another 3% uncertainty in the number of good events comes from the loss of good events due to cluster overlap in the CB. This uncertainty is associated with the correction obtained for the cluster pileup in the CB (see Sec. V A).

The overall systematic uncertainty that affects the normalization of the total and differential cross sections above 730 MeV/c is estimated to be 7%. This value is obtained by combining the systematic uncertainties listed above in quadrature. An additional uncertainty in the differential cross section arises from the finite beam–momentum resolution. Consider the experimental beam momentum distribution shown in Fig. 3. Some K^-'s from the centroid show up in the "wings" of the momentum distribution because of multiple scattering of the kaons in the beam chambers and scintillators. This effect mainly contributes to the first four and to the last two momentum intervals. We estimated this contribution to be 10 μb for the each angular bin of the differential cross section. It gives an additional 30 μb uncertainty in the total cross section.

The absolute beam momentum was obtained by assuming a linear dependence of $\sigma_{total}(K^- p \to \eta\Lambda)$ on the η momentum in the c.m. frame [see Eq. (10) below]. The uncertainty in the beam momentum is estimated to be ±2.5 MeV/c.

VIII. DISCUSSION

An inspection of Fig. 18 of $\sigma_{total}(K^- p \to \eta\Lambda)$ shows that η threshold production has a very steep onset. Pseudoscalar meson production at threshold is expected to be *s* wave. Assuming that (i) η production in the first 10 MeV/c K^- momentum above threshold is *s*-wave dominated, (ii) the matrix element is constant, and (iii) the $K^- p$ initial-state Coulomb interactions are ignorably small, we can fit the total cross section just above threshold by a simple *s*-wave production equation

$$\sigma_{total} \approx C p_\eta^*, \tag{10}$$

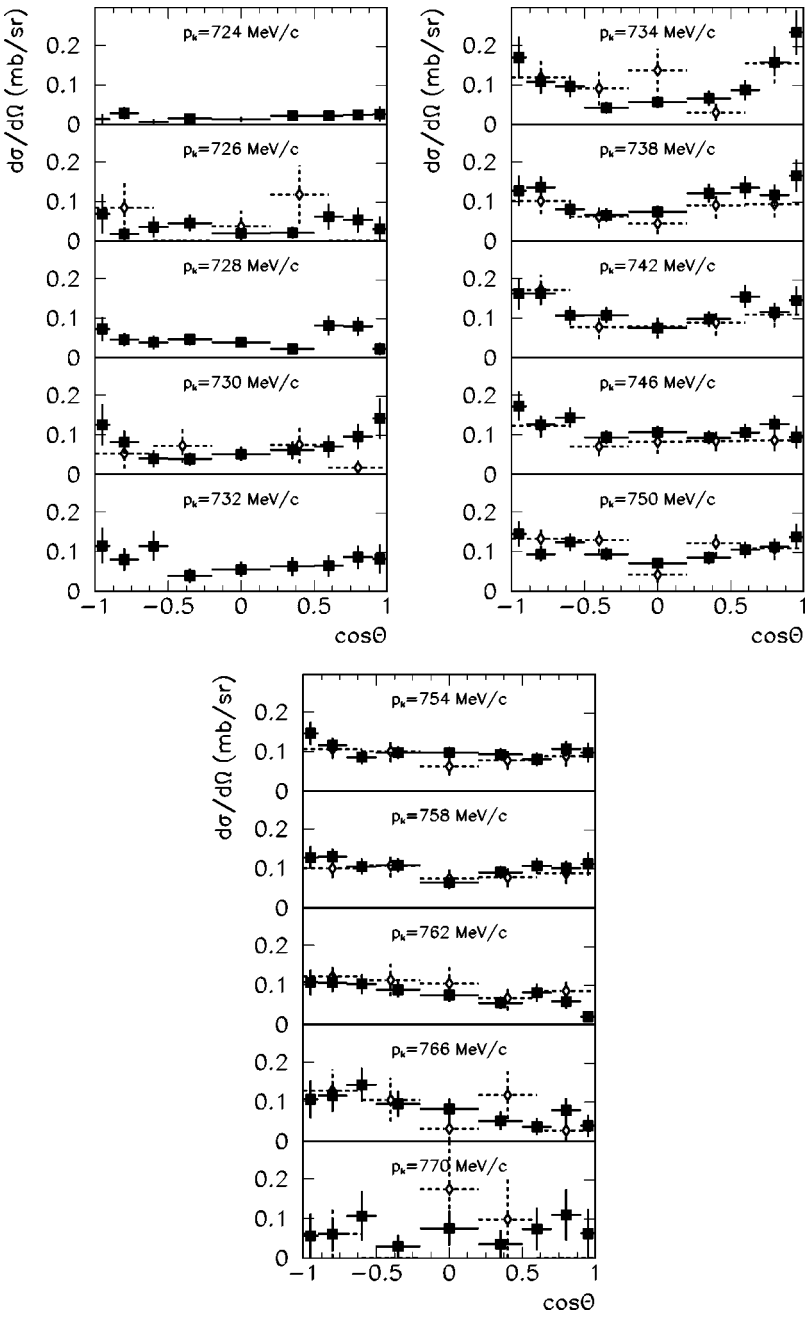

FIG. 20. $d\sigma/d\Omega(K^- p \to \eta\Lambda)$. The solid squares (■) are the differential cross sections obtained using the $\eta \to \gamma\gamma$ decay mode, the open squares (□) using $\eta \to 3\pi^0$.

where C is a constant and p_η^* is the η momentum in the c.m. The constant C is unique for each reaction and reflects the magnitude of the matrix element of the process. A one-parameter linear fit to our data from $p_\eta^* = 37$ MeV/c to $p_\eta^* = 83$ MeV/c yields

$$\sigma_{total}(K^- p \to \eta\Lambda) = (17 \pm 3)\ \ \mu\text{b}/(\text{MeV}/c) p_\eta^*, \quad (11)$$

where p_η^* is the η momentum in the c.m. in MeV/c. The uncertainty is mainly due to the uncertainty in the incident K^- momentum. The data points below $p_{K^-} = 726$ MeV/c were excluded from the fit because of their large uncertainties, both in the value of the total cross section and in the η momentum in c.m.

To understand the near-threshold η production, we assume that it is dominated by the excitation of the intermediate $\Lambda(1670)\frac{1}{2}^-$ resonance with very minor contributions from the $\Lambda(1600)\frac{1}{2}^+$ and $\Lambda(1690)\frac{3}{2}^-$ states. We parametrized the total cross section at c.m. energy E by the Breit-Wigner form,

$$\sigma_{\text{BW}}(E) = \frac{2\pi}{k^2} \frac{\Gamma_i(E)\Gamma_f(E)}{(E - E_{\text{R}})^2 + (\Gamma_{\text{tot}}/2)^2}, \quad (12)$$

where Γ_i and Γ_f are the energy-dependent partial widths for the initial and final channels, respectively, and k is the c.m.

TABLE II. $K^- p \to \eta\Lambda$ differential cross sections $d\sigma/d\Omega$ in mb/sr for beam momentum intervals of 4 MeV/c. Uncertainties are statistical only.

p_{K^-}	$\Delta \cos\Theta$								
(MeV/c)	-0.95 ± 0.05	-0.80 ± 0.10	-0.60 ± 0.10	-0.35 ± 0.15	0.00 ± 0.20	0.35 ± 0.15	0.60 ± 0.10	0.80 ± 0.10	0.95 ± 0.05
724	0.01 ± 0.01	0.03 ± 0.01	0.01 ± 0.01	0.01 ± 0.01	0.01 ± 0.01	0.02 ± 0.01	0.02 ± 0.01	0.02 ± 0.01	0.03 ± 0.02
726	0.07 ± 0.05	0.02 ± 0.02	0.04 ± 0.03	0.05 ± 0.02	0.02 ± 0.01	0.02 ± 0.01	0.06 ± 0.03	0.05 ± 0.03	0.03 ± 0.03
728	0.07 ± 0.03	0.05 ± 0.02	0.04 ± 0.02	0.05 ± 0.01	0.04 ± 0.01	0.02 ± 0.01	0.08 ± 0.02	0.08 ± 0.02	0.02 ± 0.02
730	0.13 ± 0.05	0.08 ± 0.03	0.04 ± 0.02	0.04 ± 0.02	0.05 ± 0.02	0.06 ± 0.02	0.07 ± 0.03	0.10 ± 0.03	0.14 ± 0.05
732	0.12 ± 0.04	0.08 ± 0.03	0.11 ± 0.04	0.04 ± 0.02	0.06 ± 0.02	0.06 ± 0.02	0.06 ± 0.03	0.09 ± 0.03	0.08 ± 0.04
734	0.17 ± 0.05	0.11 ± 0.03	0.10 ± 0.03	0.04 ± 0.01	0.06 ± 0.02	0.07 ± 0.02	0.09 ± 0.03	0.16 ± 0.03	0.23 ± 0.06
738	0.13 ± 0.04	0.14 ± 0.03	0.08 ± 0.02	0.07 ± 0.02	0.07 ± 0.02	0.12 ± 0.02	0.13 ± 0.03	0.12 ± 0.03	0.17 ± 0.04
742	0.16 ± 0.04	0.16 ± 0.03	0.11 ± 0.02	0.11 ± 0.02	0.08 ± 0.01	0.10 ± 0.02	0.15 ± 0.03	0.11 ± 0.02	0.15 ± 0.04
746	0.17 ± 0.04	0.13 ± 0.02	0.14 ± 0.02	0.09 ± 0.02	0.11 ± 0.02	0.09 ± 0.02	0.11 ± 0.02	0.13 ± 0.02	0.09 ± 0.03
750	0.14 ± 0.03	0.09 ± 0.02	0.12 ± 0.02	0.09 ± 0.02	0.07 ± 0.01	0.08 ± 0.01	0.10 ± 0.02	0.11 ± 0.02	0.14 ± 0.03
754	0.15 ± 0.03	0.12 ± 0.02	0.09 ± 0.02	0.10 ± 0.02	0.10 ± 0.01	0.09 ± 0.01	0.08 ± 0.02	0.11 ± 0.02	0.10 ± 0.02
758	0.13 ± 0.03	0.13 ± 0.02	0.10 ± 0.02	0.11 ± 0.02	0.06 ± 0.01	0.09 ± 0.02	0.11 ± 0.02	0.10 ± 0.02	0.11 ± 0.03
762	0.11 ± 0.03	0.11 ± 0.02	0.10 ± 0.02	0.09 ± 0.02	0.07 ± 0.02	0.05 ± 0.01	0.08 ± 0.02	0.06 ± 0.02	0.02 ± 0.01
766	0.11 ± 0.05	0.12 ± 0.04	0.14 ± 0.04	0.09 ± 0.03	0.08 ± 0.03	0.05 ± 0.02	0.04 ± 0.02	0.08 ± 0.03	0.04 ± 0.03
770	0.06 ± 0.06	0.06 ± 0.04	0.11 ± 0.06	0.03 ± 0.03	0.08 ± 0.04	0.03 ± 0.04	0.07 ± 0.05	0.11 ± 0.06	0.06 ± 0.06

momentum in the incident channel. The *s*-wave energy dependence of these partial widths was parametrized as $\Gamma_i(E)=(p^*/p^*_{\rm R})B_i\Gamma_{\rm tot}$ and $\Gamma_f(E)=(k/k_{\rm R})B_f\Gamma_{\rm tot}$, where B_i and B_f are the branching ratios for the initial and final channels, respectively, and here p^* is the c.m. momentum of the η. The pole position is given by the complex constant $E_{\rm R}-{\rm i}\Gamma_{\rm tot}/2$.

The data for the reaction $K^- p \to \eta\Lambda$ from Table I have been analyzed for the geometrical mean branching ratio $\sqrt{B_i B_f}$ and the reaction cross section σ_R at resonance (actually the pole). Rough fits are obtained by varying the resonance energy $E_{\rm R}$ and the total width $\Gamma_{\rm tot}$ to minimize the χ^2. The best fit, shown in Fig. 22, was obtained for the mass parameter $E_R=1670\pm5$ MeV, the total width $\Gamma_{tot}=24\pm4$ MeV, and the reaction cross section at the resonance energy $\sigma_R=1.3\pm0.1$ mb. The errors shown are mainly due to the uncertainty in the incident beam momentum. See Ref. [17] for further details of the analysis. A full-fledged multichannel analysis of η production and other *s* wave K^- interactions is underway by one of us (D.M.M.).

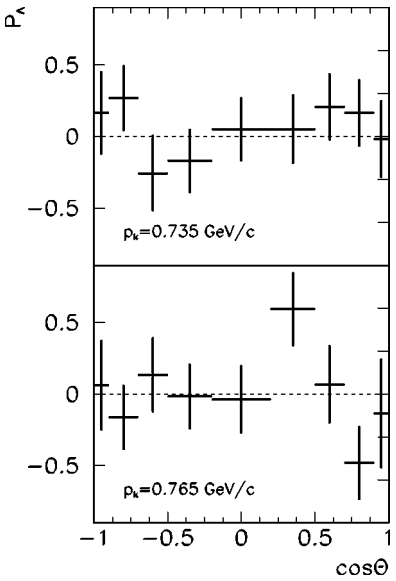

FIG. 21. The Λ polarization in $K^- p \to \eta\Lambda$ obtained using the $\eta \to \gamma\gamma$ decay mode.

The maximum value of $\sigma_{total}(K^- p \to \eta\Lambda)$ is 1.44 ± 0.10 mb at $p_{K^-}=742$ MeV/c (see Table I). This is a large cross section, given that $p^*_\eta=82$ MeV/c, which implies a small phase space compared to $\Lambda(1670)\frac{1}{2}^- \to \pi\Sigma$ with $p^*_\pi=393$ MeV/c, or $\Lambda(1670)\frac{1}{2}^- \to \bar{K}N$ with $p^*_K=414$ MeV/c.

The angular dependence of $d\sigma/d\Omega(K^- p \to \eta\Lambda)$ near threshold is consistent with *s*-wave production dominance. A simple bowl-shaped structure in the angular dependence emerges when the K^- momentum is well above threshold. It is an indication of a small *d*-wave component, presumably

TABLE III. Λ polarization in $K^- p \to \eta\Lambda$.

	p_{K^-} (MeV/c)	
$\Delta \cos\Theta$	722–750	750–770
-0.95 ± 0.05	0.16 ± 0.29	0.06 ± 0.32
-0.80 ± 0.10	0.27 ± 0.23	-0.16 ± 0.23
-0.60 ± 0.10	-0.26 ± 0.27	0.14 ± 0.26
-0.35 ± 0.15	-0.17 ± 0.22	-0.02 ± 0.23
0.00 ± 0.20	0.05 ± 0.22	-0.04 ± 0.24
0.35 ± 0.15	0.05 ± 0.24	0.59 ± 0.26
0.60 ± 0.10	0.21 ± 0.23	0.07 ± 0.27
0.80 ± 0.10	0.16 ± 0.23	-0.48 ± 0.26
0.95 ± 0.05	-0.02 ± 0.27	-0.13 ± 0.38

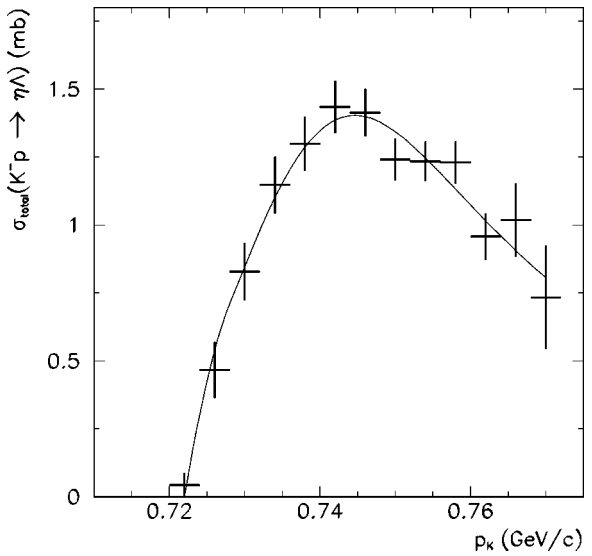

FIG. 22. The $K^-p\to\eta\Lambda$ total cross section measured for the $\eta\to\gamma\gamma$ decay mode with the high-momentum beam. The solid line is the best fit of $\sigma_{total}(K^-p\to\eta\Lambda)$ to the Breit-Wigner form of the $\Lambda(1670)\frac{1}{2}^-$ [see Eq. (12)].

from the excitation of the $\Lambda(1690)\frac{3}{2}^-$. The shape of the angular dependence for $d\sigma/d\Omega(K^-p\to\eta\Lambda)$ is similar to that for η production by π^- [4], in contrast to η production by photons [18] or protons [19]. The difference is an indication of a different reaction mechanism, e.g., photoproduction is more likely to occur via vector–meson coupling. A detailed partial-wave analysis of our $K^-p\to\eta\Lambda$ data is underway [20]. Finally, the Λ polarization at all our energies and angles is consistent with zero, as expected from *s*-wave production and $\Lambda(1670)\frac{1}{2}^-$ dominance.

IX. CONCLUSIONS

Near-threshold η production in $K^-p\to\eta\Lambda$ resembles in several respects η production in $\pi^-p\to\eta n$, namely:

(1) The steep rise in σ_{total} immediately upon the opening of the channel.

(2) *s*-wave production with similar coefficients

$$\sigma_{total}(K^-p\to\eta\Lambda)=(17\pm3)\ \ \mu\text{b}/(\text{MeV}/c)p_\eta^*, \quad (13)$$

and

$$\sigma_{total}(\pi^-p\to\eta n)=(21.2\pm1.8)\ \ \mu\text{b}/(\text{MeV}/c)p_\eta^*, \quad (14)$$

where p_η^* is the η momentum in the c.m. in MeV/c.

(3) Large total cross section near threshold

$$\max\sigma_{total}(K^-p\to\eta\Lambda)=1.44\pm0.10\ \text{mb}$$

$$\text{for}\ \ p_\eta^*=82\ \ \text{MeV}/c,$$

$$\max\sigma_{total}(\pi^-p\to\eta n)=2.60\pm0.32\ \text{mb}$$

$$\text{for}\ \ p_\eta^*=182\ \ \text{MeV}/c.$$

The SU(3) relation between these two results, $\sigma_{total}(\pi^-p\to\eta n)=4/3\times[\sigma_{total}(K^-p\to\eta\Lambda)]$, is satisfied at the expected level before a quark mass correction is applied.

(4) The angular distribution at threshold is consistent with *s*-wave dominance. Above threshold, both $d\sigma/d\Omega(K^-p\to\eta\Lambda)$ and $d\sigma/d\Omega(\pi^-p\to\eta n)$ have the same bowl-like shape in contrast to η production by photons and protons.

We conclude that η threshold production by K^- and π^- provides a striking case of the important role that flavor symmetry plays in the dynamics of strong interaction, furthermore, that breaking of flavor symmetry by the mass term in $\mathcal{L}_{QCD}$ is not serious [see Eq. (1)]. The simplest interpretation of our η threshold production data is dominance of the $\Lambda(1670)\frac{1}{2}^-$ intermediate state, but a mixture of more than one state is not excluded. The successful application of $SU(3)_f$ symmetry to the $N(1535)\frac{1}{2}^-$ and $\Lambda(1670)\frac{1}{2}^-$ states implies that both resonances are three-quark states and that the $N(1535)\frac{1}{2}^-$ is not a $K\Sigma$–$K\Lambda$ bound state as proposed in the literature [7].

ACKNOWLEDGMENTS

We wish to thank SLAC for the use of the Crystal Ball (CB) detector, which enabled us to make accurate, efficient, and fast measurements. We appreciate the care given to the CB during its storage at SLAC by E. Bloom, G. Godfrey, and J. Broder. Special thanks go to G. Godfrey for his role in the reactivation of the CB and his sage advice. We appreciate the support of the AGS, in particular we acknowledge P. Pile and J. Scaduto for their help with the installation and the beamline support. We gratefully acknowledge L. Jia for the design, construction, and installation of the liquid-hydrogen target. We thank R. Chrien and the BNL medium energy group for supplying the beam chambers and assistance during the experiment. We acknowledge stimulating discussions with V. V. Abaev. This experiment was supported in part by the U.S. DOE and NSF, NSERC of Canada, the Russian Ministry of Industry, Science and Technologies, the Russian Foundation for Basic Research, and a sabbatical support (H.M.S.) by the Volkswagen Stiftung of Germany.

[1] G. Miller, B. Nefkens, and I. Slaus, Phys. Rep. **194**, 1 (1990).
[2] D. M. Binnie *et al.*, Phys. Rev. D **8**, 2789 (1973).
[3] M. Clajus and B. M. K. Nefkens, πN Newsletter **7**, 76 (1992).
[4] B. M. K. Nefkens and A. B. Starostin, Acta Phys. Pol. B **31**, 2669 (2000).
[5] V. V. Abaev and B. M. K. Nefkens, Phys. Rev. C **53**, 385 (1996).
[6] D. E. Groom *et al.*, Eur. Phys. J. C **15**, 401 (2000).

[7] N. Kaiser, P. Segal, and W. Weise, Phys. Lett. B **362**, 23 (1995).
[8] G. W. London *et al.*, Nucl. Phys. **B85**, 289 (1975).
[9] D. F. Baxter *et al.*, Nucl. Phys. **B67**, 125 (1973).
[10] R. Rader *et al.*, Nuovo Cimento Soc. Ital. Fis., A **16A**, 178 (1973).
[11] D. Berley *et al.*, Phys. Rev. Lett. **15**, 641 (1965).
[12] W. B. Tippens *et al.*, Phys. Rev. D **63**, 052001 (2001).
[13] E. D. Bloom and C. W. Peck, Annu. Rev. Nucl. Sci. **33**, 143 (1983).
[14] CODA: A. Scalable, Distributed Data Acquisition System, W. A. Watson III, J. Chen, G. Heyes, E. Jastrzembski, and D. Quarrie, IEEE Trans. Nucl. Sci. **41**, 61 (1993).
[15] V. Bekrenev and A. Kulbardis, Crystal Ball Note CB-99-012, 1999, on http://bmkn8.physics.ucla.edu/Crystalball
[16] R. Armenteros *et al.*, Nucl. Phys. **B21**, 23 (1970).
[17] Chun Wa Wong, Crystal Ball Note CB-01-001, 2001, on http://bmkn8.physics.ucla.edu/Crystalball
[18] B. Krusche *et al.*, Phys. Rev. Lett. **74**, 3736 (1995).
[19] H. Calen *et al.*, Phys. Lett. B **458**, 190 (1999).
[20] A. Gårdestig (unpublished).